Superenhancement Photon Upconversion Nanoparticles for Photoactivated Nanocryometer

Qiqing Li, Xiaoyu Xie, Han Wu, Haoran Chen, Wang Wang, Xianggui Kong, and Yulei Chang*

Cite This: *Nano Lett.* 2023, 23, 3444−3450

Read Online

ACCESS | Metrics & More | Article Recommendations | SI Supporting Information

ABSTRACT: Highly doped lanthanide luminescent nanoparticles exhibit unique optical properties, providing exciting opportunities for many ground-breaking applications, such as super-resolution microscopy, deep-tissue bioimaging, confidentiality, and anticounterfeiting. However, the concentration-quenching effect compromises their luminescence efficiency/brightness, hindering their wide range of applications. Herein, we developed a low-temperature suppression cross-relaxation strategy, which drastically enhanced upconversion luminescence (up to 2150-fold of green emission) in Er^{3+}-rich nanosystems. The cryogenic field opens the energy transport channel of Er^{3+} multiphoton upconversion by further suppressing phonon-assisted cross-relaxation. Our results provide direct evidence for understanding the energy loss mechanism of photon upconversion, deepening a fundamental understanding of the upconversion process in highly doped nanosystems. Furthermore, it also suggests the potential applications of upconversion nanoparticles for extreme ambient-temperature detection and anticounterfeiting.

KEYWORDS: *upconversion, cryogenic field, cross-relaxation, thermometer, anticounterfeiting*
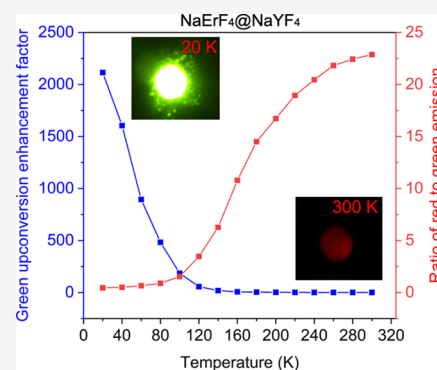
Lanthanide-doped upconversion nanomaterials (UCNPs) can convert the pumping near-infrared (NIR) photons to ultraviolet, visible even at high-energy NIR emissions, which have aroused great interest for a wide range of applications such as bioimaging,[1−3] photoinduced therapy,[4−6] super-resolution,[7,8] and optical thermometry.[9] However, the luminescence efficiency of UCNPs still limits their wide applications. Recently, various strategies have been developed to improve their brightness, such as core−shell coating,[10] dye sensitization,[11] a dry synthesis method,[12] plasma enhancement,[13] etc. However, due to the influence of concentration quenching, defects and impurities, and density of phonon states, the excitation energy is apt to dissipate in high-lying levels, the doping concentration of UCNPs is insufficient, and the luminous efficiency cannot be further improved.

In concentration quenching, the luminescence intensity decreases with an increase in dopant concentration. This is a crucial factor that limits the luminescence efficiency of UCNPs.[14,15] Two aspects that led to concentration quenching are energy migration among the same ions to the surface defects and cross-relaxation (CR) between dopant ions, which depopulate the high-energy population state to the low-energy population state.[16] With an increase in dopant ion concentration, the distance between adjacent ions decreases and the CR process intensifies, which dramatically decreases the radiative transition rate in high-energy levels and attenuates the overall emission intensity. Studies have also attempted to address concentration-quenching effects such as high-density excitation[17,18] and epitaxial inert shells,[19] but there has not been

substantial progress. Since 2017, we and other researchers have reported $NaErF_4@NaYF_4(NaLuF_4)$ NPs,[20,21] which has deepened the understanding of the luminescence mechanism; this is typically considered impossible in bulk materials. The emerging new formulation of doping with a high content of Er^{3+} has the characteristics of multiwavelength excitation and near-monochromatic red light, enabling a simple structure design for multicolor regulation in photoswitchable UCNPs.[4,22] However, there is a lack of further in-depth systematic research on the luminescence mechanism in addition to suppressing the excited-state energy and preventing the rapid migration to the surface defects.

Furthermore, compared with $NaYF_4:2\%Er@NaYF_4$, the absorption of $NaErF_4@NaYF_4$ increased by 50 times, but the luminescence intensity did not improve to the same extent.[23] These results indicated that the nonradiative (NR) energy transfer (or CR) mechanism is dominant in the concentration quenching, which has not yet been investigated. CR generally comprises phonon-assisted and resonance CR (PACR and RCR),[24] which occurred with and without an energy mismatch during energy transfer. Considering that the energy gap (ΔE)
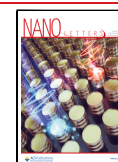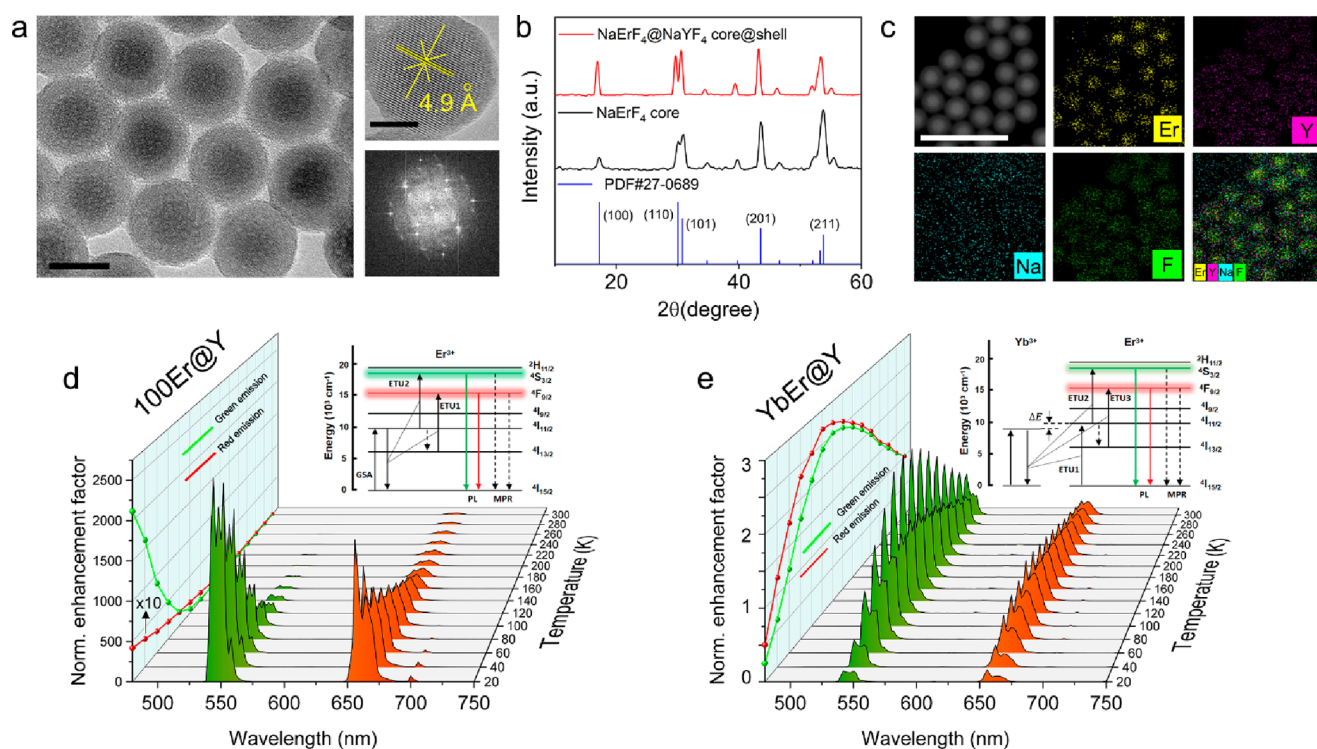
Figure 1. (a) Transmission electron microscopy (TEM) image (left), high-resolution TEM image (top right), and corresponding Fourier-transform diffraction pattern (bottom right) of the NaErF$_4$@NaYF$_4$ core−shell UCNPs. (b) XRD patterns of the NaErF$_4$ core and NaErF$_4$@NaYF$_4$ core−shell samples. (c) Element mappings of Er, Y, and their overlap for the sample in (a). (d, e) Temperature-dependent upconversion emission spectra obtained from samples NaErF$_4$@NaYF$_4$ and NaYF$_4$:20%Yb,2%Er@NaYF$_4$ nanoparticles, respectively, under 980 nm excitation.

between Er^{3+} energy levels is not equally spaced, phonon-assisted CR is bound to occur during the upconversion process.[25] The phonon absorption and emission rates are determined by the number density of phonons, which is proportional to the temperature. That is to say, at a higher temperature, there is an inevitable increase in the NR energy transfer process, especially the CR process, effectively enhanced due to the increase in lattice vibration or phonons, which could weaken the emission intensity. This phenomenon is called thermal quenching. Thus, we hypothesize that the cryogenic field could delay the thermal quenching, further resulting in suppressing the concentration quenching.

Herein, to confirm the above hypothesis, we investigated the luminescence process of NaErF$_4$-based UCNPs by steady-state and time-resolved spectroscopy at cryogenic fields. At low temperatures, the CR process was significantly suppressed, which significantly enhanced the UCL, especially in the green bands, by 2 orders of magnitude (2150-fold). In addition, with a decrease in temperature, the thermochromism of 100Er@Y varied from monochromatic red and yellow to green. Moreover, the red-to-green (R/G) light ratio changed from 23 to 0.45, suggesting that the concentration quenching of green emissions was suppressed, which, to the best of our knowledge, has never been reported in the codoped systems. We used this excellent feature to demonstrate its application in low-temperature detection in extreme environments and temperature anti-counterfeiting.

Cryogenics is crucial in exploring the luminescence mechanism and can be used to design multicolor UCL behavior. To clearly reveal the fundamental photophysical process, especially the role of the CR process in Er^{3+}-rich self-sensitized UCNPs in the cryogenic field, we synthesized typical NaErF$_4$

core and NaErF$_4$@NaYF$_4$ core−shell UCNPs (100Er@Y) using coprecipitation and decomposition methods, respectively.[26] TEM images in Figure 1a show that the monodispersed core−shell UCNPs have spherical shapes in sizes of 25 ± 3.1 nm. The X-ray diffraction (XRD) patterns in Figure 1b indicate the hexagonal phase of the as-obtained UCNPs according to the standard card (JCPDS file number 27-0689), demonstrating that the shell grew isotropically on the nanoparticle surface (Figure 1b). Energy dispersive spectrometry (EDS) images in Figure 1c and the electron energy loss spectroscopy analysis in Figure S1 clearly show the spatial distributions of Er^{3+} and Y^{3+} ions separately, further confirming the successful preparation of the core@shell nanostructured UCNPs.

To examine the influence of low temperature on the UCL of Er^{3+}-rich NPs, we measured the emission spectra of 100Er@Y NPs under 980 nm excitation at different temperatures (from 20 to 300 K). As shown in Figure 1d, the overall UCL intensities showed a monotonous increasing trend with decrease in temperature; moreover, typical green and red UCL emission bands at 540 and 650 nm, respectively, were obtained in the low-temperature region (20−160 K), corresponding to the $^4S_{3/2} \rightarrow {}^4I_{15/2}$ and $^4F_{9/2} \rightarrow {}^4I_{15/2}$ transitions of Er^{3+}, respectively. The CIE coordinates showed a noticeable emission color change from red to yellow and finally to green with a decrease in temperature (Figure S2). The proposed UC mechanism under 980 nm excitation is illustrated in Figure 1d (upper diagram). Er^{3+} ions were pumped from the ground state to the $^4I_{11/2}$ level through a ground-state absorption process and transitioned to higher $^4F_{9/2}$ and $^4S_{3/2}$ levels through an energy transfer (ET) process. Compared to the near-monochromatic red emissions around room temperature, the integrated intensities of green and red UCL were enhanced by more than 2150 and 40 times,
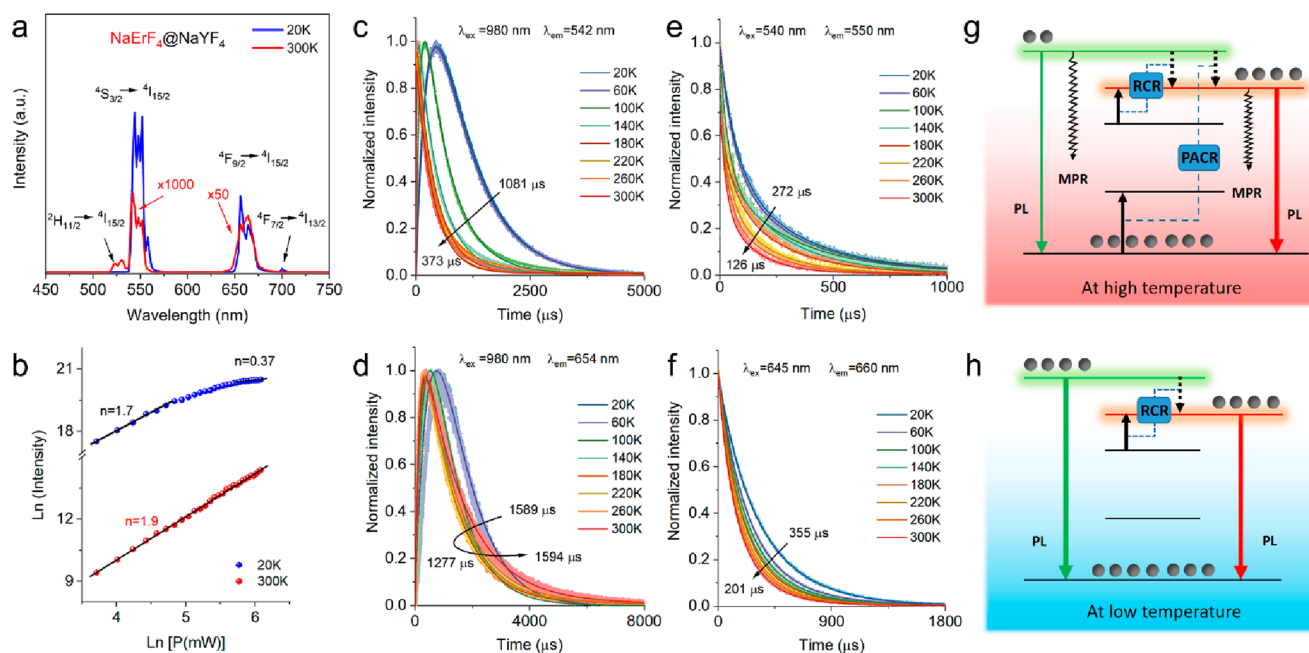
Figure 2. (a) UCL spectra of 100Er@Y NPs at 20 and 300 K. (b) Excitation power dependence of green UCL of 100Er@Y under different excitation powers at 980 nm. (c, d) Time resolution UCL intensities at 542 nm and 654 nm, respectively, at different temperatures upon 980 nm excitation. (e, f) Time resolution DSL intensities at 550 nm excited by 540 nm and at 660 nm excited by 645 nm, respectively. (g, h) Sketches of population and depopulation processes of 100Er@Y NPs at high and low temperatures, respectively. Abbreviations: RCR, resonance cross relaxation; PACR, phonon-assisted cross relaxation; MPR, multiphonon relaxation; PL, photoluminescence.

respectively (Figure 1d, left chart). Furthermore, the enhancement factors have trends similar to that of 980 nm excitation under 800 or 1530 nm (Figure S3), but the maximum enhancement factors are different due to the different population mechanisms in the upconversion process. This sharp green light enhancement differed from traditional codoped Yb/Er UCNPs.

As shown in Figure 1e, the UCL intensity of $NaYF_4$:20% $Yb,2\%Er@NaYF_4$ (YbEr@Y) first increased and then decreased with decreasing temperature. This phenomenon occurred because of the competition between MPR and phonon-assisted energy transfer upconversion (ETU) processes, consistent with a previous report.[27] Specifically, according to eq S2, when the temperature decreased from 300 to 180 K, MPR was mitigated, resulting in a decreased energy loss of excited states, which was conducive to the increase in UCL. When the temperature decreased from 180 to 20 K, the effect of reduced phonon-assisted ETU of the $Yb^{3+} \rightarrow Er^{3+}$ process exceeded that of decreased MPR, resulting in the loss of energy population and then a decline in the UCL intensity. In YbEr@Y NPs, the ETU from Yb^{3+} to Er^{3+} is the dominant population process, while the ETU from Er^{3+} to Er^{3+} is the domain population of 100Er@Y. Therefore, energy transfer between Er−Er is the key to study the abnormal enhancement of UCL in 100Er@Y. The underlying mechanisms are discussed in the dynamics section.

Specifically, we investigated the UCL of 100Er@Y NPs at 20 and 300 K (Figure 2a). The integrated emission intensity at 20 K is approximately 2150 and 42 times that at 300 K for green and red UCL, respectively. Since $^2H_{11/2}$ and $^4S_{3/2}$ are thermally coupled energy states, the 520 nm emission of $^2H_{11/2}$ was observed at high-temperature regions, and the ratio of 520 to 542 nm emission intensity decreased with decreasing temperature. However, the 520 nm emission almost disappeared below 140 K, implying that the maximum phonon energy was smaller

than the energy gap between $^4S_{3/2}$ and $^2H_{11/2}$ states and could not transfer electrons from the lower to the higher energy level (Figure S4). Furthermore, with increasing temperature, the emission bands of 100Er@Y NPs show an abnormal blue shift with broadening bandwidth due to phonon broadening. For example, the full width at half maxima of emission peak at 542 nm increases when the temperature increases, as shown in Figure S5. To study the effect of temperature on the UCL, the output slopes for 542 nm UCL were measured, as shown in Figure 2b. As discussed in Section 3.2.1 in the Supporting Information, the slope of UCL, which depends on pumping power density P, could become decreasingly smaller with increasing population of the intermediate state. At 20 K, the slopes gradually decreased from 1.7 to 0.37 with increasing power density, indicating that the population of the $^4I_{11/2}$ intermediate state was enhanced and approached saturation at lower excitation power densities. As shown in Figure S6a,b, the downshifting luminescence (DSL) of the $^4I_{11/2}$ state increased when the temperature decreased, which intuitively showed the enhancement effect of low temperature on the population of the $^4I_{11/2}$ intermediate state. For red UCL, the slope decreased with a decrease in temperature at a relatively high excitation power (Figure S7). These results confirmed that lower temperatures boosted the populations of the Er^{3+} excited states, enhancing the UCL.

To study the effect of cryogenic field on the dynamic process of UCL, the luminescence decays of 100Er@Y at 542 nm were measured under the excitation of a 980 nm pulse laser (Figure 2c). In fact, UCL is a nonlinear process, and the dynamic process of UCL can be simply divided into population and depopulation. The population process is mainly determined by the ground-state absorption and the ETU from donor to acceptor, and the depopulation process is determined by luminescence and NR (including MPR and CR). Due to these multiple transition and
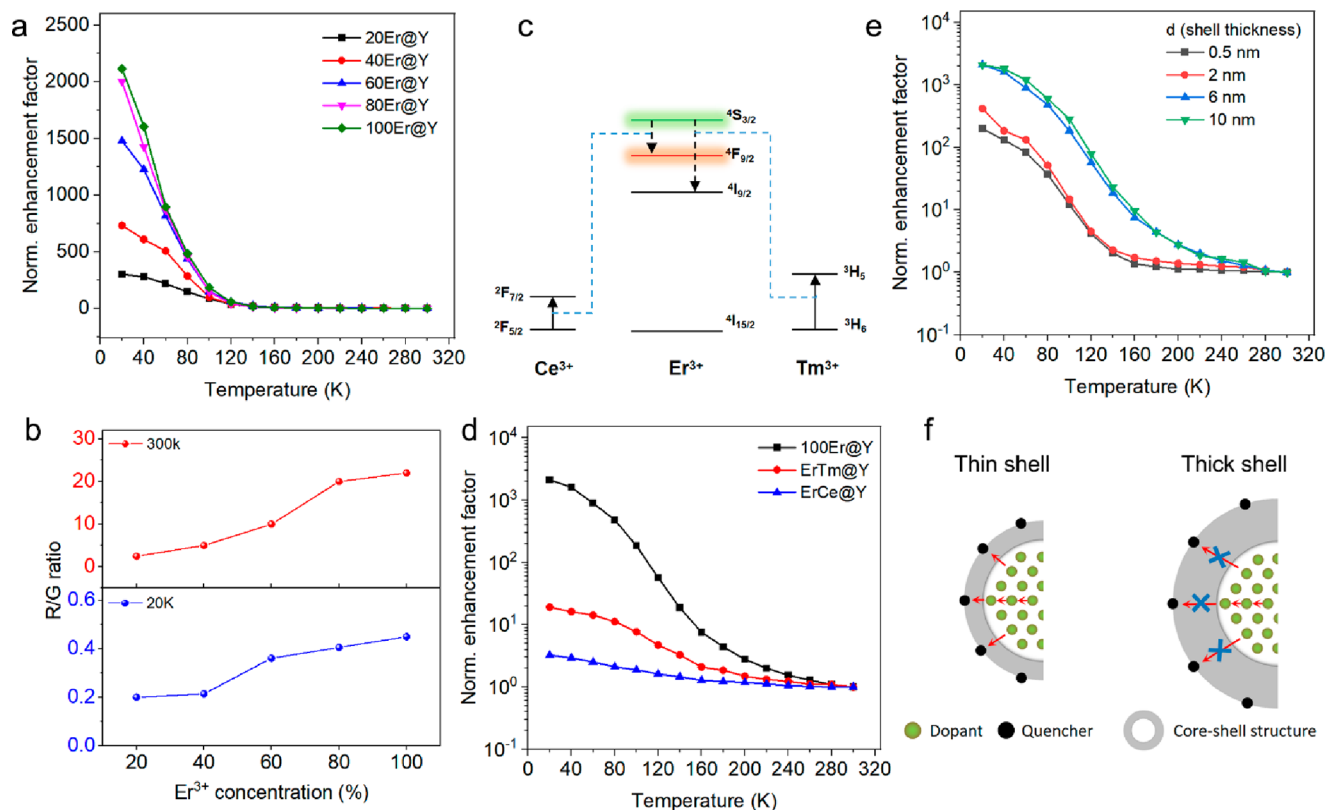
Figure 3. (a) Temperature dependence of the green upconversion enhancement factor from the xEr@Y core−shell nanoparticles with different Er^{3+} concentrations upon 980 nm excitation. (b) R/G ratio of xEr@Y versus different Er^{3+} concentrations at 20 K (bottom) and 300 K (top). (c) Schematic CR processes between Er^{3+} and other dopant ions (Ce/Tm) from the samples in ErTm@Y and ErCe@Y UCNPs. (d) Temperature dependence of the green upconversion enhancement factor from the $NaErF_4$:Ln@Y core−shell nanoparticles with different dopant ions (Ln = Tm, red line; Ln = Ce, blue line) under 980 nm excitation. (e) Temperature dependence of the green upconversion enhancement factor from the Er@Y core−shell nanoparticles with different shell thicknesses upon 980 nm excitation. (f) Schematic energy migration from the lanthanide dopant to surface quencher in 100Er@Y with a thin shell (left) or a thick shell (right).

relaxation processes, the temporal dependencies of UCL present double-exponential or triple-exponential decay. As discussed in section 3.2.2 in the Supporting Information, the lifetime of the UCL at 542 nm was calculated using eq 1:

$$I(t) = A_0 + A_1 e^{-t/\tau_1} + A_2 e^{-t/\tau_2} \tag{1}$$

The upconversion decay curve had two parts, rise time and decay time, which were determined by the minimum and maximum values of τ_1 and τ_2, respectively. The average lifetime τ_{ave} of UCL was calculated using eq 2:

$$\tau_{ave} = \frac{\int_0^\infty \tau I(t)\, dt}{\int_0^\infty I(t)\, dt} = \frac{A_1 \tau_1^2 + A_2 \tau_2^2}{A_1 \tau_1 + A_2 \tau_2} \tag{2}$$

Table S1 shows the calculated 542 nm UCL lifetimes fitted by eqs 1 and 2. A predictable decline in lifetime τ_{ave} from 1081 to 373 μs was observed, and the rising edge gradually disappeared with increasing temperature (Figure 2c). Thus, the decreasing lifetime of the $^4S_{3/2}$ state helped reduce the UCL due to the increasing NR relaxation with increasing temperature. For the $^4F_{9/2}$ state of 654 nm, the upconversion lifetime was influenced by the lifetime of $^4I_{11/2}$ and $^4I_{13/2}$ states (eq S7). The lifetime τ_{ave} first decreased from 1589 to 1277 μs (from 20 to 180 K) and then increased to 1594 μs (300 K) (Figure 2d and Table S2), while the luminescence intensity decreased monotonically. This nonmonotonicity of lifetime was attributed to the increasing energy migration among the $^4F_{9/2}$ levels of Er^{3+} ions with

increasing temperature, which increased the lifetime of red UCL at the high-temperature range (180−300 K).[28] However, the UCL intensities of 542 and 654 nm were greatly enhanced at low temperatures, while their corresponding UCL lifetimes were only slightly prolonged. This because the UCL intensities are not proportional to the corresponding decay time (eqs S4 and S9), but they are all related to NR rate ($\beta_4 + \gamma_4$).

Due to the upconversion process involving multiple intermediate energy levels, the specific effect of the cryogenic field on MPR and CR cannot be clarified directly by the decay of UCL. Unlike upconversion decay, downshifting decay only involves a depopulating process, which can straightforwardly demonstrate the changes in MPR and CR. Therefore, to thoroughly investigate this unique phenomenon of prolonged lifetimes of UCL at the cryogenic field, temperature-dependent DSL decay curves of 100Er@Y were also obtained upon excitation at 540 and 650 nm (Figure 2e,f, respectively). The temperature dependence of DSL decay was determined by the radiative decay rate (α), MPR rate (β), and CR rates (γ) using eq 3[29,30]

$$\tau(c, T) = \frac{1}{\alpha + \beta(T) + \gamma(c, T)} \tag{3}$$

where c is the doping concentration of Er^{3+} ions and T is the temperature. According to the decay curves in Figure 2e, close to biexponential decay occurred instead of single-exponential decay (see details in Section 3.2.3 in the Supporting
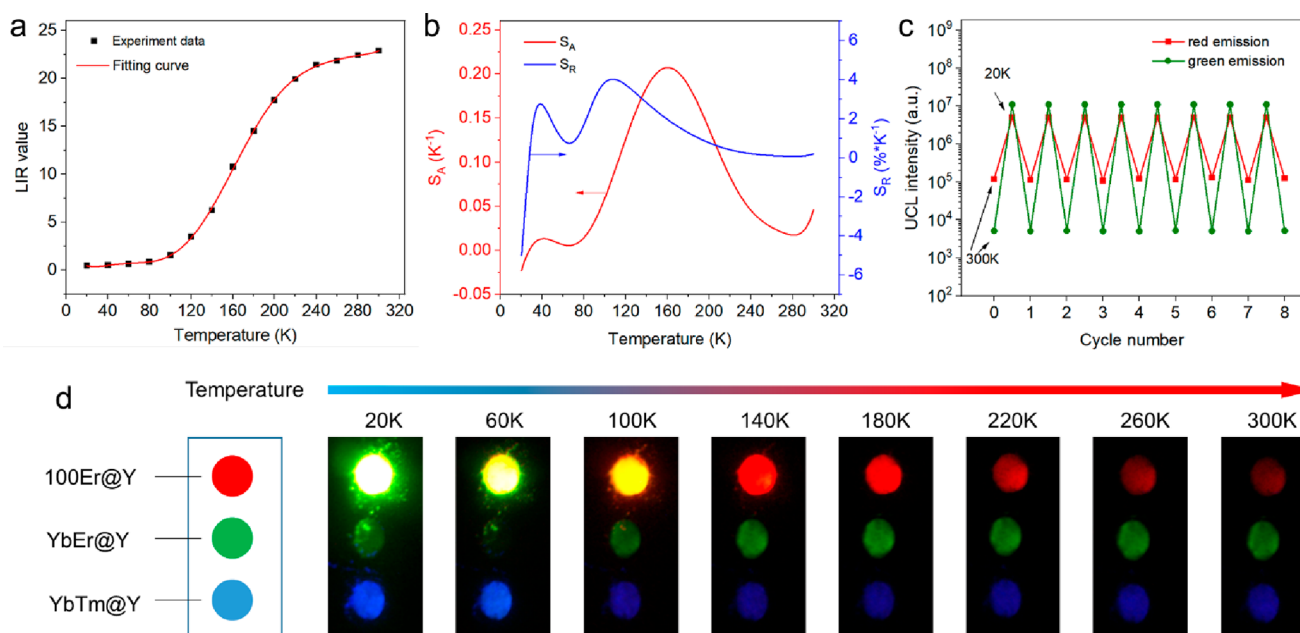
Figure 4. (a) Temperature-dependent LIR value of UCL and (b) corresponding absolute sensitivity (S_A) and relative sensitivity (S_R) for the 100Er@Y core−shell nanoparticles under 980 nm excitation. (c) Thermal cycling measurements for the upconversion emission intensity of 100Er@Y at 542 and 654 nm between 20 and 300 K. (d) Visible images of a temperature indicator composed of three types of NPs (100Er@Y:NaErF$_4$@NaYF$_4$, red disk; YbEr@Y:NaYF$_4$:20%Yb,2%Er@NaYF$_4$, green disk; YbTm@Y:NaYF$_4$:25%Yb,0.5%Tm@NaYF$_4$, blue disk) at different temperatures.

Information). Therefore, the average lifetime τ_{ave} of the DSL for 100Er@Y was calculated using eq 2, as shown in Table S3. The results showed that the lifetime of the $^4S_{3/2}$ state (550 nm) decreased from 272 to 126 μs, indicating the growing NR relaxation process (MPR and CR) with increasing temperature.

To obtain the quantitative analysis of CR, the DSL decay curve at 550 nm for NaYF$_4$:1%Er@NaYF$_4$ (1Er@Y) was measured (Figure S8). The values of CR and NR rates of the $^4S_{3/2}$ state in 1Er@Y and 100Er@Y calculated by the eqs S14 and S15 are presented in Tables S3 and S4, respectively. At 300 K, the NR and CR rates of 100Er@Y were 6.78×10^3 and 5.59×10^3 s^{-1}, respectively, suggesting that the extensive CR dominated the depopulation of the $^4S_{3/2}$ state and led to the extremely weak green UCL at room temperature (red/green = 23/1) (Figure 2g). At 20 K, the NR rate was close to the CR rate, indicating that the MPR process had almost disappeared; however, the CR process still existed in 100Er@Y (Figure 2g,h). With decreasing temperature, the number of phonons in the host decreased, which reduced the phonon-assisted MPR and PACR processes ($^4S_{3/2} + {}^4I_{15/2} \rightarrow {}^4F_{9/2} + {}^4I_{13/2}$), and the RCR process ($^4S_{3/2} + {}^4I_{9/2} \rightarrow 2{}^4F_{9/2}$) did not require phonon assistance, which could occur at very low temperatures. The DSL lifetime of the $^4F_{9/2}$ state (660 nm) changed from 355 to 201 μs when the temperature increased from 20 to 300 K because the NR rate increased from 0.63×10^3 to 2.79×10^3 s^{-1} (Figure 2f and Table S5). Overall, these results confirmed that the significant enhancement of UCL (especially green emission) in 100Er@Y could be attributed to the significant suppression of the CR process at low temperatures (<100 K).

To better understand the effect of CR on the thermal quenching of Er^{3+}-rich UCNPs, the temperature-dependent UCL of NaYF$_4$:x%Er@NaYF$_4$ (xEr@Y) with different Er^{3+} doping concentrations (x = 20, 40, 60, 80 and 100) was investigated (characterization in Figure S9). As shown in Figure 3a, the enhancement factor of 540 nm UCL at 20 K increased from 264 to 2150 as the Er^{3+} doping concentration increased

from 20% to 100%, and the enhancement factor of 650 nm UCL intensity increased from 23 to 42 (Figure S10). According to the Förster−Dexter equation, the ET rate is inversely proportional to the sixth power of the distance between the activator and the sensitizer.[31] Therefore, the closer distance between the activator and the sensitizer can enhance the ETU process in Figure 1d, achieving a larger enhancement factor. In addition, at 300 K, the luminescence intensity ratio (LIR) of the red-to-green UCL in the xEr@Y UCNPs increased from 2.5 to 23 with an increase in Er^{3+} doping concentration (upper chart in Figure 3b and Figure S11), indicating that the green UCL was quenched by the CR process (Figure 1e). However, at 20 K, the LIR of 100Er@Y was still larger than that of xEr@Y with low doping concentration (Figure 3b, lower chart), suggesting the existence of a CR process in 100Er@Y. Furthermore, we designed and prepared a set of control samples to investigate the effect of CR on enhancing UCL. For example, we introduced a small amount of impurities (e.g., 0.5% Tm or 0.5% Ce) into the NaErF$_4$ sublattice to enhance the CR process:[23,32] $^3H_6$ (Tm^{3+}) + $^4S_{3/2}$ (Er^{3+}) $\rightarrow {}^3H_5$ (Tm^{3+}) + $^4F_{11/2}$ (Er^{3+}) or $^2F_{5/2}$ (Ce^{3+}) + $^4S_{3/2}$ (Er^{3+}) $\rightarrow$ $^2F_{7/2}$ (Ce^{3+}) + $^4F_{9/2}$ (Er^{3+}) (Figure 3c). As shown in Figure 3d, the upconversion enhancement factors of NaErF$_4$:0.5%Tm@ NaYF$_4$ (ErTm@Y) and NaErF$_4$:0.5%Ce@NaYF$_4$ (ErCe@Y) at lower temperature decreased considerably, confirming that the CR process led to weak green UCL. To investigate the effect of shell thickness on thermal quenching, the temperature-dependent UCL of 100Er@Y with different thicknesses was measured. Figure 3e shows that a thicker shell helped achieve a larger enhancement factor due to the decreased surface quenching. With a thinner shell layer, the sample suffers from more surface quenching because of energy migration from the core to the surface (Figure 3f).

The anomalous thermosensitive UCL in the 100Er@Y core−shell nanoparticles indicated their promising applications in noncontact nanothermometry. However, as mentioned above, the 520 nm UCL disappeared when the temperature was below

140 K upon 980 nm excitation; thus, the ratio of the UCL intensity of the thermally coupled $^2H_{11/2}$ and $^4S_{3/2}$ levels cannot be used as a thermometer at ultralow temperatures. Therefore, we explored the LIR of the $^4F_{9/2}$ to $^4S_{3/2}$ states for ultralow temperature sensing. Further, we examined the thermometry performance of 100Er@Y in the range 20−300 K. Based on the rate equation discussed in Section 3.3.4 in the Supporting Information, we obtained the mathematical expression of the R/G ratio using eq S16. The LIRs from these two levels were fitted using a polynomial function (Figure 4a). Finally, the absolute sensitivities (S_A) and relative sensitivities (S_R) were determined as follows:

$$S_A(T) = \frac{dLIR}{dT} \tag{4}$$

$$S_R(T) = \frac{S_A}{LIR} \times 100\% \tag{5}$$

The corresponding S_A and S_R are plotted in Figure 4b. The maximum S_R was 4% K^{-1} at 115 K, higher than those for other reported lanthanide-doped NPs for low-temperature detection (Table S6). Furthermore, the thermoresponsive UCL showed good stability and reversible performance (Figure 4c), indicating that our proposed material is an ideal candidate as a robust cryogenic engineering material for noncontact low-temperature sensing. Based on the anomalous thermosensitive upconversion emissions of 100Er@Y UCNPs, we also demonstrated the application of thermoresponsive optical information security and anticounterfeiting (Figure 4d). Compared to common UCNPs of YbEr@Y and YbTm@Y, both the intensity and the visual colors of UCL of 100Er@Y changed with an increase in temperature, resulting in a color change from green and yellow to red (supplementary video 1). Although the intensities of the contrast sample also changed (Figure 1e and Figure S12), the visual color did not change.

In summary, we demonstrated an upconversion nanoprobe based on highly erbium-doped UNCPs for ultralow-temperature detection and anticounterfeiting. The suppression of CR considerably enhanced the green upconversion at low temperatures, resulting in a high relative sensitivity of up to 4% K^{-1} using the red and green UCL. Furthermore, the temperature-dependent intensity and lifetimes of UCL and DSL revealed the role of MPR and CR in highly doped nanoparticles, providing more dimensional control for mitigating concentration quenching. This study provides a general approach for designing highly sensitive thermal probes for ultralow temperature sensing, and it also offers deep insights into the photophysics involving the UCL behavior of lanthanides in cryogenics.

■ ASSOCIATED CONTENT

ⓈⒾ Supporting Information

The Supporting Information is available free of charge at (PDF) The Supporting Information is available free of charge at https://pubs.acs.org/doi/10.1021/acs.nanolett.3c00495.

> Experimental section, characterization methods, theoretical analysis of upconversion process, lement mapping, fluorescence spectra, pump power dependence of UCL, and UCL lifetimes for different samples, temperature-dependent enhancement factor for different samples, tables of calculated parameters (PDF)

> Visual colors of UCL of 100Er@Y changomg with an increase in temperature (MP4)

■ AUTHOR INFORMATION

Corresponding Author

Yulei Chang − *State Key Laboratory of Luminescence and Applications, Changchun Institute of Optics, Fine Mechanics and Physics, Chinese Academy of Sciences, Changchun 130033 Jilin, People's Republic of China;* ⓞ orcid.org/0000-0001-7223-1797; Email: yuleichang@ciomp.ac.cn

Authors

Qiqing Li − *State Key Laboratory of Luminescence and Applications, Changchun Institute of Optics, Fine Mechanics and Physics, Chinese Academy of Sciences, Changchun 130033 Jilin, People's Republic of China*

Xiaoyu Xie − *State Key Laboratory of Luminescence and Applications, Changchun Institute of Optics, Fine Mechanics and Physics, Chinese Academy of Sciences, Changchun 130033 Jilin, People's Republic of China*

Han Wu − *State Key Laboratory of Luminescence and Applications, Changchun Institute of Optics, Fine Mechanics and Physics, Chinese Academy of Sciences, Changchun 130033 Jilin, People's Republic of China*

Haoran Chen − *State Key Laboratory of Luminescence and Applications, Changchun Institute of Optics, Fine Mechanics and Physics, Chinese Academy of Sciences, Changchun 130033 Jilin, People's Republic of China*

Wang Wang − *State Key Laboratory of Luminescence and Applications, Changchun Institute of Optics, Fine Mechanics and Physics, Chinese Academy of Sciences, Changchun 130033 Jilin, People's Republic of China*

Xianggui Kong − *State Key Laboratory of Luminescence and Applications, Changchun Institute of Optics, Fine Mechanics and Physics, Chinese Academy of Sciences, Changchun 130033 Jilin, People's Republic of China*

Complete contact information is available at:
https://pubs.acs.org/10.1021/acs.nanolett.3c00495

Author Contributions

Q.L. and X.X. contributed equally to this work. Q.L. and Y.C. conceived and designed the experiments. Y.C. supervised the project. X.X., Q.L., and H.W. synthesized the nanoparticles. X.X., Q.L., W.W., and H.W. conducted the optical experiments and characterizations. Q.L., X.X., X.K., and Y.C. prepared the figures and conducted the data analysis. Q.L. and Y.C. wrote the paper, with input from all authors.

Notes

The authors declare no competing financial interest.

■ REFERENCES

(1) Zhong, Y.; Ma, Z.; Zhu, S.; Yue, J.; Zhang, M.; Antaris, A. L.; et al. Boosting the down-shifting luminescence of rare-earth nanocrystals for biological imaging beyond 1500 nm. *Nat. Commun.* **2017**, *8* (1), 737.

(2) Gu, Y.; Guo, Z.; Yuan, W.; Kong, M.; Liu, Y.; Liu, Y.; et al. High-sensitivity imaging of time-domain near-infrared light transducer. *Nat. Photonics.* **2019**, *13* (8), 525−531.

(3) Fan, Y.; Wang, P.; Lu, Y.; Wang, R.; Zhou, L.; Zheng, X.; et al. Lifetime-engineered NIR-II nanoparticles unlock multiplexed in vivo imaging. *Nat. Nanotechnol.* **2018**, *13* (10), 941−946.

(4) Chen, H.; Wu, F.; Xie, X.; Wang, W.; Li, Q.; Tu, L.; et al. Hybrid Nanoplatform: Enabling a Precise Antitumor Strategy via Dual-Modal Imaging-Guided Photodynamic/Chemo-/Immunosynergistic Therapy. *ACS Nano* **2021**, *15* (12), 20643−20655.

(5) Liu, B.; Chen, Y. Y.; Li, C. X.; He, F.; Hou, Z. Y.; Huang, S. S.; et al. Poly(Acrylic Acid) Modification of Nd^{3+}-Sensitized Upconversion Nanophosphors for Highly Efficient UCL Imaging and pH-Responsive Drug Delivery. *Adv. Funct. Mater.* **2015**, *25* (29), 4717−4729.

(6) Zhang, Z.; Jayakumar, M. K. G.; Zheng, X.; Shikha, S.; Zhang, Y.; Bansal, A.; et al. Upconversion superballs for programmable photo-activation of therapeutics. *Nat. Commun.* **2019**, *10* (1), 4586.

(7) Liu, Y. J.; Lu, Y. Q.; Yang, X. S.; Zheng, X. L.; Wen, S. H.; Wang, F.; et al. Amplified stimulated emission in upconversion nanoparticles for super-resolution nanoscopy. *Nature* **2017**, *543* (7644), 229.

(8) Zhan, Q. Q.; Liu, H. C.; Wang, B. J.; Wu, Q. S.; Pu, R.; Zhou, C.; et al. Achieving high-efficiency emission depletion nanoscopy by employing cross relaxation in upconversion nanoparticles. *Nat. Commun.* **2017**, *8*, 1058.

(9) Yan, L.; Huang, J.; An, Z.; Zhang, Q.; Zhou, B. Activating Ultrahigh Thermoresponsive Upconversion in an Erbium Sublattice for Nanothermometry and Information Security. *Nano Lett.* **2022**, *22* (17), 7042−7048.

(10) Chen, X.; Jin, L.; Kong, W.; Sun, T.; Zhang, W.; Liu, X.; et al. Confining energy migration in upconversion nanoparticles towards deep ultraviolet lasing. *Nat. Commun.* **2016**, *7*, 10304.

(11) Zou, W. Q.; Visser, C.; Maduro, J. A.; Pshenichnikov, M. S.; Hummelen, J. C. Broadband dye-sensitized upconversion of near-infrared light. *Nat. Photonics.* **2012**, *6* (8), 560−564.

(12) Homann, C.; Krukewitt, L.; Frenzel, F.; Grauel, B.; Wurth, C.; Resch-Genger, U.; et al. NaYF$_4$:Yb,Er/NaYF$_4$ core/shell nanocrystals with high upconversion luminescence quantum yield. *Angew. Chem., Int. Ed.* **2018**, *57*, 8765−8769.

(13) Wu, Y.; Xu, J.; Poh, E. T.; Liang, L.; Liu, H.; Yang, J. K. W.; et al. Upconversion superburst with sub-2 mus lifetime. *Nat. Nanotechnol.* **2019**, *14* (12), 1110−1115.

(14) Dexter, D. L.; Schulman, J. H. Theory of concentration quenching in inorganic phosphors. *J. Chem. Phys.* **1954**, *22* (6), 1063−1070.

(15) Wang, J.; Deng, R.; MacDonald, M. A.; Chen, B.; Yuan, J.; Wang, F.; et al. Enhancing multiphoton upconversion through energy clustering at sublattice level. *Nat. Mater.* **2014**, *13* (2), 157−162.

(16) Chang, Y.; Chen, H.; Xie, X.; Wan, Y.; Li, Q.; Wu, F.; et al. Bright Tm^{3+}-based downshifting luminescence nanoprobe operating around 1800 nm for NIR-IIb and c bioimaging. *Nat. Commun.* **2023**, *14* (1), 1079.

(17) Zhao, J.; Jin, D.; Schartner, E. P.; Lu, Y.; Liu, Y.; Zvyagin, A. V.; et al. Single-nanocrystal sensitivity achieved by enhanced upconversion luminescence. *Nat. Nanotechnol.* **2013**, *8* (10), 729−734.

(18) Benz, F.; Strunk, H. P. Rare earth luminescence: A way to overcome concentration quenching. *AIP Adv.* **2012**, *2* (4), 042115.

(19) Chen, G.; Shen, J.; Ohulchanskyy, T. Y.; Patel, N. J.; Kutikov, A.; Li, Z.; et al. (alpha-NaYbF$_4$:Tm^{3+})/CaF$_2$ core/shell nanoparticles with efficient near-infrared to near-infrared upconversion for high-contrast deep tissue bioimaging. *ACS Nano* **2012**, *6* (9), 8280−8287.

(20) Zuo, J.; Li, Q.; Xue, B.; Li, C.; Chang, Y.; Zhang, Y.; et al. Employing shells to eliminate concentration quenching in photonic upconversion nanostructure. *Nanoscale* **2017**, *9* (23), 7941−7946.

(21) Johnson, N. J.; He, S.; Diao, S.; Chan, E. M.; Dai, H.; Almutairi, A. Direct Evidence for Coupled Surface and Concentration Quenching Dynamics in Lanthanide-Doped Nanocrystals. *J. Am. Chem. Soc.* **2017**, *139* (8), 3275−3282.

(22) Zuo, J.; Tu, L.; Li, Q.; Feng, Y.; Que, I.; Zhang, Y.; et al. Near Infrared Light Sensitive Ultraviolet-Blue Nanophotoswitch for

Imaging-Guided "Off-On" Therapy. *ACS Nano* **2018**, *12* (4), 3217−3225.

(23) Yan, L.; Zhou, B.; Song, N.; Liu, X.; Huang, J.; Wang, T.; et al. Self-sensitization induced upconversion of Er^{3+} in core-shell nanoparticles. *Nanoscale* **2018**, *10* (37), 17949−17957.

(24) Tarelho, L. V. G.; Gomes, L.; Ranieri, I. M. Determination of microscopic parameters for nonresonant energy-transfer processes in rare-earth-doped crystals. *Phys. Rev. B* **1997**, *56* (22), 14344−14351.

(25) Miyakawa, T.; Dexter, D. L. Phonon sidebands, multiphonon relaxation of excited states, and phonon-assisted energy transfer between ions in solids. *Phys. Rev. B* **1970**, *1* (7), 2961−2969.

(26) Xie, X.; Li, Q.; Chen, H.; Wang, W.; Wu, F.; Tu, L.; et al. Manipulating the Injected Energy Flux via Host-Sensitized Nanostructure for Improving Multiphoton Upconversion Luminescence of Tm^{3+}. *Nano Lett.* **2022**, *22* (13), 5339−5347.

(27) Wu, K.; Cui, J.; Kong, X.; Wang, Y. Temperature dependent upconversion luminescence of Yb/Er codoped NaYF$_4$ nanocrystals. *J. Appl. Phys.* **2011**, *110* (5), 053510.

(28) Zuo, J.; Sun, D.; Tu, L.; Wu, Y.; Cao, Y.; Xue, B.; et al. Precisely Tailoring Upconversion Dynamics via Energy Migration in Core-Shell Nanostructures. *Angew. Chem., Int. Ed.* **2018**, *57* (12), 3054−3058.

(29) Eldridge, J. I. Luminescence decay-based Y$_2$O$_3$:Er phosphor thermometry: Temperature sensitivity governed by multiphonon emission with an effective phonon energy transition. *J. Lumin.* **2019**, *214*, 116535.

(30) Wadhwa, A.; Wang, C.; Wang, C.; Ma, R.; Qiao, X.; Fan, X.; et al. Multi-phase glass-ceramics containing CaF$_2$: Er^{3+} and ZnAl$_2$O$_4$:Cr^{3+} nanocrystals for optical temperature sensing. *J. Am. Chem. Soc.* **2018**, *102* (5), 2472−2481.

(31) Wu, P. G.; Brand, L. Resonance Energy Transfer: Methods and Applications. *Anal. Biochem.* **1994**, *218* (1), 1−13.

(32) Chen, Q.; Xie, X.; Huang, B.; Liang, L.; Han, S.; Yi, Z.; et al. Confining Excitation Energy in Er^{3+}-Sensitized Upconversion Nanocrystals through Tm^{3+}-Mediated Transient Energy Trapping. *Angew. Chem., Int. Ed.* **2017**, *56* (26), 7605−7609.

⬚ Recommended by ACS